Experiments and Lagrangian simulations on the formation of droplets in drop-on-demand mode

J. R. Castrejón-Pita,[1] N. F. Morrison,[2] O. G. Harlen,[2] G. D. Martin,[1] and I. M. Hutchings[1]
[1]*Institute for Manufacturing, University of Cambridge, Cambridge, CB3 0FS, United Kingdom*
[2]*Department of Applied Mathematics, University of Leeds, Leeds, LS2 9JT, United Kingdom*
(Received 1 June 2010; revised manuscript received 2 November 2010; published 11 March 2011)

The creation and evolution of millimeter-sized droplets of a Newtonian liquid generated on demand by the action of pressure pulses were studied experimentally and simulated numerically. The velocity response within a model, large-scale printhead was recorded by laser Doppler anemometry, and the waveform was used in Lagrangian finite-element simulations as an input. Droplet shapes and positions were observed by shadowgraphy and compared with their numerically obtained analogues.

DOI: 10.1103/PhysRevE.83.036306 PACS number(s): 47.55.db, 47.80.Jk

I. INTRODUCTION

The rigorous study of the formation of droplets began with the theoretical models and experiments of Rayleigh, Plateau, and Savart in the 19th century [1–3]. In recent decades, the study of droplets has received much attention in the context of several industrial applications, including inkjet printing. The technological advances behind modern commercially available printers allow the production of drops on demand of a diameter down to few micrometers at several meters per second [4]. Although these characteristics are satisfactory for many important applications such as large-scale printing and labeling, they are inadequate for others such as the printing of conductive tracks or of transistors for electronics applications. The major challenges of the printing industry are numerous and varied, but there are certain fundamentals. Some of the starting points are the behavior of satellite droplets and the speed of drop motion as both affect the quality of printing.

Most drop-on-demand (DoD) printheads work either by the action of piezoelectric transducers or by the use of heating elements to create droplets. For piezoelectric printheads, meticulous acoustical characterization of the printhead interior and the liquid is required in order to achieve the greatest possible efficiency in amplifying the action produced by the piezoelectric elements [5]. In contrast, bubble-jet printheads use heaters to vaporize part of the ink, creating an expanding bubble that causes the ejection of the droplet [6]. The heating elements used in bubble-jet technology can be microintegrated in the manufacturing process, and as a consequence these printheads can be packed more closely than in a piezoelectric type, achieving higher resolution. The disadvantage of bubble-jet technology is that it is compatible only with certain liquids. Despite these points, both technologies are restricted to jetting liquids within a limited viscosity range. Regardless of which technology is used, other concerns are faced by printing. The faster the liquid is jetted, the more likely is the production of droplets with longer ligaments trailing back toward the nozzle. These ligaments are undesirable as they typically fragment into small "satellite" drops that are difficult to control or predict and can degrade the quality of printing. In addition to these difficulties, the characterization of the ejection of viscoelastic fluids from DoD printheads is a topic that has to be studied and controlled before the technology may be applied reliably to biomaterials, polymers, and metallic particles [7]. Although major advances in the experimental and theoretical understanding of the formation of liquid ligaments, droplets, and jets have been achieved in the past century, it is generally accepted that many problems remain unsolved, particularly in the field of droplet jetting and breakup [8,9]. The study of the behavior of droplets is not only relevant to graphical inkjet printing but also to any process where droplet formation is used as a way to deliver liquid materials. Current applications include the generation of DNA arrays, the creation of organic transistors and diodes, the deposition of ceramics and polymers, and microdispensing applications [10–12].

Although detailed experimental and numerical data exist on the internal dynamics of particular printheads [13–15], applications are often driven by empirical results rather than by analytical or numerical models. The reasons for this are the complexities and limitations of both approaches in defining or reproducing the jetting conditions in a given printhead. This is justified because the conditions inside modern commercially available printheads are difficult to measure, as their small physical dimensions and high operating speeds do not admit the direct measurement or observation of the jetting and liquid conditions before and during the formation of the droplets. As a consequence, most studies have been based on the observation of droplets in flight, during deposition, or after drying on the substrate.

The observation and characterization of droplets produced by commercially available systems is complicated. This is due to the physical size of the systems and to the speed of printing: High-resolution and high-speed imaging are always required for these studies, [10,12,16]. A large-scale system offers several advantages over these commercial counterparts. First, the dynamics of a Newtonian fluid can be reproduced at lower speeds by matching the relevant dimensionless numbers, i.e., the Reynolds and Weber numbers. In addition, the physical size of a scaled-up version of a drop generator facilitates the use of experimental techniques such as laser Doppler anemometry, flow meters, and pressure transducers to measure properties such as pressure, speed, and temperature within the printhead reservoir and the fluid close to the nozzle.

Commonly, experimental studies of DoD systems aim to investigate the effects of the electrical input signal on the jet breakup and the formation of satellite droplets [17]. A similar process is often followed to optimize the operating conditions required to eject a fluid at a certain jet or drop speed with a

minimum number of satellites. The studies presented in this work intend to go further by also studying the internal fluid velocity and pressure.

In this paper, a description is given of a large-scale experimental setup that is capable of reproducing the jetting conditions of micrometer-scale DoD printheads, by adjusting the properties of the jetted liquid and the jetting conditions. The apparatus allows the direct measurement of several properties that are unavailable in other designs, such as the dynamic pressure, the liquid velocity above the nozzle plane, the position of the meniscus within the nozzle, and the evolution dynamics of the jetted droplets. These characteristics produce a system where most of the jetting conditions are known and controllable, and which is therefore suitable to be modeled numerically. Based on measurements of the fluid velocity, Lagrangian numerical simulations were performed in order to test the ability of the code to replicate the behavior of droplets. Shadowgraph images obtained from the experimental setup with a 2 mm nozzle are compared with their numerically simulated counterparts. The inputs to the Lagrangian simulations are the driving velocity pulse (obtained by laser Doppler anemometry from the experimental setup), the nozzle geometry, and the liquid properties.

II. EXPERIMENTAL DETAILS

A. Drop-on-demand generator

The large-scale droplet generator employed here is capable of producing droplets on demand from nozzles with diameters ranging from 250 μm up to 4 mm and is designed to reproduce the fluid mechanical conditions relevant to a typical commercial inkjet printhead. The basic system has been described elsewhere [18]; briefly, it uses an electrodynamic actuator (a loudspeaker) to produce pressure pulses that eject liquid through a nozzle. The system is illustrated in Fig. 1.

The complete system contains two liquid reservoirs, one inside the printhead above the nozzle, and another larger one that is open to the atmosphere. The largest container has two purposes: to feed liquid into the printhead and to control the position of the meniscus of liquid on the nozzle plane. The static pressure within the printhead is given by the

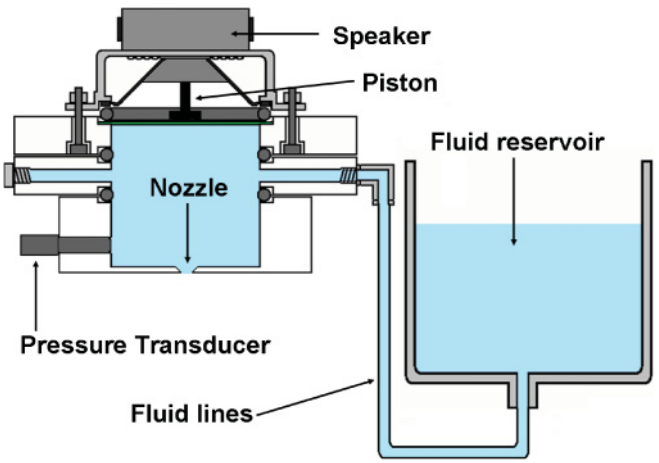

FIG. 1. (Color online) Schematic diagram of the DoD generator. Components not to scale.

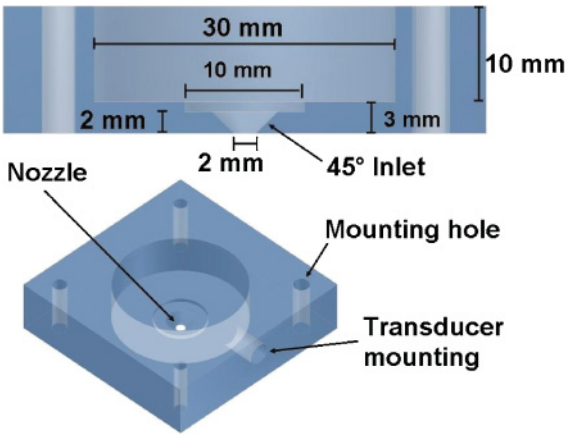

FIG. 2. (Color online) Dimensions of the nozzle machined in perspex for the present work. Dimensions in scale.

effective column head of the liquid in the external reservoir. The meniscus is held at the nozzle plane by adjusting the height of the fluid reservoir. The liquid in the printhead is in contact with a 0.05 mm thick brass membrane on the top, with the nozzle on the bottom, and with a calibrated fast-pressure transducer (Entran Sensors & Electronics, EPX-N12-1B, full specifications in Ref. [19]) on one side, as shown in Fig. 1. The printhead body is made of transparent PMMA (Plexiglass, Perspex) to allow optical access to the printhead and the direct observation of the liquid meniscus inside the nozzle. The nozzle was machined out of a 3 mm PMMA sheet to a precision of 50 μm and consists of a conical inlet 2 mm deep with a final diameter of 2 mm. The detailed geometry of the nozzle is shown in Fig. 2.

The ejection of droplets is achieved by the displacement of the loudspeaker cone and the membrane in response to an electric signal. In commercial applications the driving waveform requires detailed characterization, as (for a given ink and printhead geometry) it directly controls the droplet shape, speed, volume, and number of satellite droplets in the printing process [20]. In this work, simple driving waveforms consisting of single 15 V square pulses of 5–15 ms duration were used. It was found that pulses shorter than 5 ms do not produce ejection, whereas pulses longer than 15 ms introduce air into the printhead. Waveforms were produced by a TTi TGP110 pulse generator and amplified to 15 V by a TTi WA301 wide-band amplifier. Synchronous with the waveform, a delay generator (Stanford Research Systems Inc. DG535) was triggered to set the timing interval between the droplet ejection and the visualization system.

B. Visualization

The optimal operating conditions of commercial printheads are found by empirical studies where the formation and deposition of droplets are usually observed by optical means [17,21]. In a similar way, in the present experiments, shadowgraphy was used to capture snapshots of the ejection process at various times. Two visualization systems were used separately: single-flash photography and high-speed imaging. Single-flash photography was used primarily for the shape analysis of droplets, on the grounds of its superior image

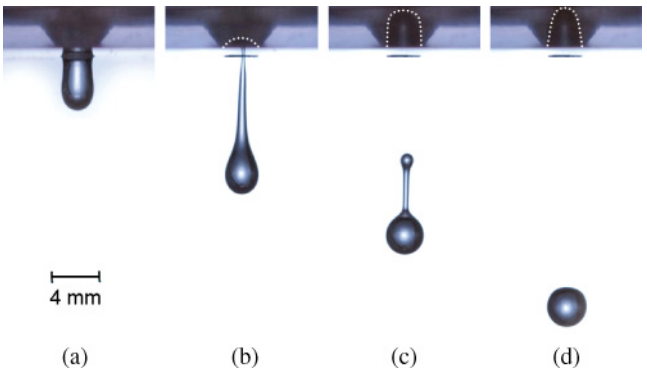

FIG. 3. (Color online) Single-flash photographs taken at various times, each capturing a separate droplet. Image (a) was taken approximately 6 ms after the pulse had been sent to the actuator, (b) at 18 ms, (c) at 27 ms, and (d) at 36 ms. Potential timing errors of up to 2 ms are associated with these values. Detachment from the printhead occurred at 20 ms but the position of the meniscus inside the nozzle is discernible from 12 ms onward. The interface of the meniscus is marked by a white dotted line.

resolution. High-speed imaging was used to provide additional data for quantitative comparison with the simulations, due to its better timing accuracy.

For the single-flash photography, a Nikon Speedlight flash (model SB-800) was used as a light source to back-illuminate the jet through a 20 cm × 20 cm acrylic diffuser. Flash pulses were triggered by a relay activated by the waveform driving the actuator in the printhead, with a response time of 5 ms. The jetting sequence was built up by taking pictures of successive events, by delaying the flash pulse. This time delay was controlled by the aforementioned delay generator. Images were recorded by a D80 Nikon camera (10.2 Megapixels CCD with a vibration reduction 18–135 mm lens). The flash was used with the 1/128 setting to produce light pulses of approximately 24 μs duration. The camera shutter was opened for 1.5 seconds with a sensitivity of ISO 400. These experiments were made in a darkened room, so the exposure time was determined by the flash duration and not by the shutter speed. The camera lens arrangement was adjusted to produce a field of view of 5.0 cm × 7.5 cm and a depth of field of approximately 10 mm. Under these conditions, single-flash images permitted the direct observation of the meniscus inside the printhead, and the process of droplet ejection; some examples are shown in Fig. 3. The final image resolution for this setup was 45.5 pixels/mm.

High-speed imaging was performed with an ultra-high-speed Shimadzu HPV–1 monochrome camera with a Nikon 24–85 mm f 2.8 zoom lens. The camera has a fixed resolution of 312 × 260 pixels and was used at a frame separation of 0.2 ms. The illumination for this setup was provided by a continuous 500 W filament lamp placed 1.5 m away from the printhead. A 30 cm × 30 cm acrylic diffuser was positioned 15 cm away from the printhead and in front of the lamp to produce an even image background. The camera lens was adjusted to produce a field of view of 104 mm × 86 mm, and thus the image resolution was 3 pixels/mm. Experiments with ultra-high-speed imaging and single-flash systems with very high resolution have been used in the past to visualize micrometer-sized droplets in flight [12,17]. In such experiments, for example, resolutions down to 0.6 μm/pixel were achieved to permit imaging of droplets with diameters of a few micrometers. Although the absolute resolution (in μm/pixel) attained in the present study is poorer, the field of view of the overall image is much wider, so that the effective resolution (i.e., the number of pixels that form a feature on an image) is significantly greater than that in previous studies. In this work, a droplet typically has a diameter of 130 pixels in the digitally recorded image.

C. Fluid and ejection conditions

Glycerol-water mixtures provide a good model system for Newtonian fluids as their viscosities can range from 1 mPa s to 1.5 Pa s with only small variation in surface tension [10,22,23]. The fluid used in all the experiments was a mixture of 85% glycerol (99.9% pure) with 15% triple-distilled water with a mixture density of $\rho = 1222$ kg m^{-3} (measured by weighing a 100 ml sample on a Sartorius scale, BP211D), a surface tension of $\sigma = 0.064$ N m^{-1} (measured with a bubble pressure tensiometer SITA Messtechnik), and a viscosity of $\eta = 0.1$ Pa s (measured by a Visco-lite 700 viscometer, Hidramotion). All the experiments were performed at 20°C.

These fluid properties, the diameter of the nozzle (d = 2 mm), and the speed of the droplet upon reaching a steady near-spherical shape ($v \approx 0.66$ m s^{-1}) were carefully chosen to match the conditions of operation of a generic commercial DoD printhead for which the nozzle diameter is typically 50 μm and the drop speed is around 6 m s^{-1}; in this way, both systems have similar dynamics. The matching was characterized by the Reynolds (Re) and Weber (We) numbers, which are defined as

$$\mathrm{Re} = \frac{\rho d v}{2\eta}, \qquad \mathrm{We} = \frac{\rho d v^2}{2\sigma}.$$

Under these conditions the system exhibits a Reynolds number of Re = 8.1 and Weber number of We = 8.3. Commonly, another dimensionless number that contrasts the importance of viscous and surface tension forces, the Ohnesorge number, is also used [24]. The Ohnesorge number is defined as $\mathrm{Oh} = \sqrt{\mathrm{We}}/\mathrm{Re}$, and for this system its value is Oh = 0.36.

It should be noted that although the Reynolds and Weber numbers in the large-scale experiments were matched to those of a commercial printhead, there are other dimensionless groups that it was not realistically possible to match; in particular, the Froude number (see Sec. III A) and the Bond number ($\mathrm{Bo} = \rho g d^2/4\sigma$), both of which quantify the importance of gravity in the flow. Thus gravity plays a relatively stronger role when the nozzle diameter is increased, and in this sense the large-scale model is not entirely perfect in its representation of the dynamics of a commercial printhead.

D. Laser Doppler anemometry

The mechanism behind the formation of droplets in piezoelectric actuator printheads is based on the conversion of an electrical drive waveform (usually a single pulse or a series of pulses) into a pressure or velocity wave that ejects the fluid from a nozzle. Detailed experiments on the effect of the driving waveform on the jetting behavior have been conducted using commercially available printheads [10]. Other studies

have been carried out where the velocity waveform is modeled in various ways, such as by square pulses and segmented sinusoids [11,23,25]. However, experiments have shown that the drive waveform may differ significantly from the fluid velocity wave produced by the action of the actuators [13]. Numerical or theoretical studies of the effect of a real, measured fluid pressure or speed wave on jetting have not been performed previously.

In the experimental setup described above, the imaging techniques combined with the optical properties of the printhead allow visualization of the meniscus motion and the formation of the droplets in response to pressure pulses. The fluid velocity data, the initial meniscus position, and the liquid properties are all inputs for the Lagrangian simulations and as a consequence had to be independently measured. Laser Doppler anemometry (LDA) was used to measure the velocity inside the printhead, and its results were used as a boundary condition in the numerical code.

LDA is a widely used nonintrusive technique in fluid dynamics that has been employed in the study of droplets formed by the breakup of jets [26,27]. Briefly, LDA determines the speed of seeding particles through the collection of scattered light produced by the interaction of a laser interference pattern with these particles; a complete description can be found in Ref. [28]. In practice, the size of the seeding particles is chosen in accordance with the dynamic conditions of the flow, as they must be able to follow the flow accurately. The behavior of the seeding particles in the flow is calculated using Stokes's law to derive the limiting frequency:

$$f_{\text{Stokes}} < \frac{0.1\eta}{\rho_p R^2}, \tag{1}$$

where ρ_p is the density and R the radius of the particles. Equation (1) determines the limiting frequency (and consequently the period) for which the particles follow a change in the flow with a deviation of up to 1% [29,30]. For the particles used in these experiments (Dantec 10 μm silver-coated glass spheres), f_{Stokes} was less than 10 MHz.

The system used in these experiments was a backscattering one-dimension Dantec LDA mounted in a Dantec three - axis automatic stage [31]. Although usually an overestimate, the size of the LDA measurement volume is generally determined by the waist of the lasers in the crossing [26–28], which was $36 \times 300 \times 36\ \mu\text{m}^3$ for the system used here. An image of the intersecting laser beams used to measure the flow within the printhead is shown in Fig. 4.

LDA is ideal for measuring speed in constant or steady laminar flows, but its use is not straightforward in conditions where the flow is oscillatory or turbulent [31]. The acquisition of LDA data can be complicated under conditions where sudden changes of the flow speed occur, because the operating parameters in commercial LDA are usually chosen by the user to identify Doppler signals from a specific velocity range, and to reject any others. This characteristic is very useful for filtering noise and enhancing the acquisition rate, but if left uncontrolled it may cause the loss of important flow information. In addition to this complication, the data obtained by LDA are not equally distributed in time, as a velocity measurement is conditioned to the presence of particles inside the measurement volume, which is a random process. The data acquisition rate is dependent on the flow speed, as in a fast flow more particles pass across the measurement volume per unit of time than in a slow one. In flows with large velocity variations (e.g., turbulence) this feature produces data that are far from being equally spaced in time, as most data are captured during periods of high speed. In such circumstances, the data generated by LDA may be reconstructed to allow certain analyses, among others the fast Fourier transform [30]. In this work, the LDA data were reconstructed using a simple accumulation method.

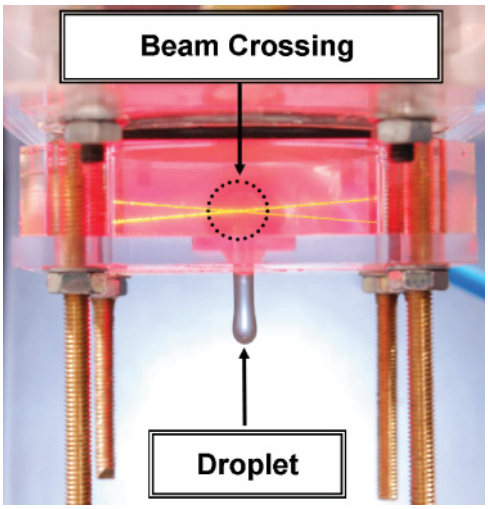

FIG. 4. (Color online) The experimental apparatus with the LDA lasers aligned in their measurement position above the nozzle.

The waveform generator (TTi TGP110 pulse generator) was adjusted to produce single square pulses every 12 s with an accuracy of 50 ns. After amplification, these pulses were sent to the loudspeaker to produce single droplets. The resulting precision of the repeatability of the pressure pulses (and thus the formation of droplets) was determined to be better than 20 μs (mostly due to the response time of the loudspeaker). It was observed that a time of 5 seconds was needed for the meniscus to return to the nozzle plane. The longer repetition time of 12 s was chosen to ensure that the system had recovered its internal dynamic conditions before each new pulse. Each pressure pulse was monitored and recorded by a digital TDS-2004B Tektronix oscilloscope at an acquisition rate of 50 kHz. Pressure pulses were continually compared and no noticeable differences were found, confirming the repeatability of the dynamic conditions inside the printhead.

LDA was used to measure the vertical component of the fluid velocity at a position 5.6 mm above the nozzle as shown in Fig. 4 and was set up to acquire data for 60 s. As a consequence, each run contained velocity data for five pressure pulses, separated by 12 s. On average, a data rate of 1000 velocity measurements per second was obtained. Although this acquisition rate is enough to identify the presence of the pulses, it was not enough to observe individual pulse details. A reconstructed pulse was obtained by dividing the data into periods equal to the time separating the pulses (12 s) and then accumulating these into a single period. This method aims to fill the gaps in the velocity measurements by assuming that different periods have different information.

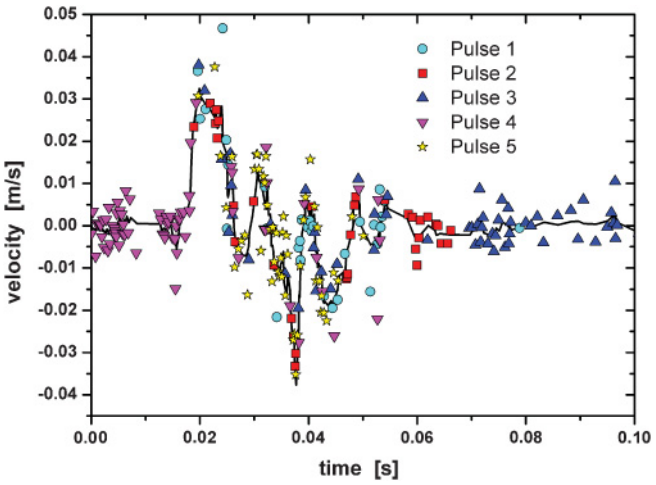

FIG. 5. (Color online) Accumulation of LDA measurements within a single period of 12 s. Different symbols indicate data from different periods. The solid line is the result of a five-point average of the accumulated data along the horizontal axis.

After the reconstruction by accumulation, a five-point average was applied to the data; typical results are shown in Fig. 5. The accumulated LDA data were then used as an input in the simulations.

III. SIMULATION DETAILS

Numerical simulations of Newtonian jetted droplets have been used to study the effects of dimensionless variables on the dynamics of the droplets with some success [9,11,25]. In these previous studies, a model velocity waveform is usually chosen as the jetting driver. Generally, two approaches are commonly modeled: capillary dripping and jetting, driven by a model pressure waveform. In the first category simulations and experimental studies have been carried out where a droplet is formed from a vertical capillary by a constant fluid flow. In this approach, the dimensionless groups are set by adjusting the flow rate and/or the fluid properties [21]. In the second category, droplet formation is produced on demand by modeling a conjectured velocity waveform [9,11,25]. Although the latter approaches are very useful to understand the effect of a pressure wave on drop formation, they are still limited as the dynamics inside a real printhead are generally unknown. In the present simulations actual waveforms measured by LDA, as described in the previous section, were used for the boundary conditions, and the results from the model were directly compared with the experimental measurements.

A. Numerical method

Lagrangian and finite-element methods have been previously employed to study the contraction and deformation of free liquid filaments in terms of viscosity and surface tension forces with some success [16,24]. These studies established that low-viscosity fluid filaments contract faster than those with high viscosity. In early studies, a critical value of the Ohnesorge number (Oh) was proposed to identify the point in which the process of a drop breaking away from the end of the filament starts to occur [16,24]. Later studies found that a contracting fluid filament with Oh $>$ O(0.1) does not break up, whereas a filament with Oh $<$ O(0.1) does break [16]. Although these investigations showed qualitative agreement with experimental observations and may represent the drop formation from dripping capillaries, these simulations encounter some limitations on cases where the drop is formed by fast jetting [16]. This is because these studies assumed an idealized problem with simplifications generally not observed in faster DoD jetting [22]. The numerical simulations presented in this work aim to provide a framework whereby the experimentally obtained dynamics of the jetting process are used to model the behavior of droplet creation and evolution.

The numerical simulations used a finite-element method first developed for the study of creeping flow of dilute polymer solutions [32]. The method has since been extended to deal with inertial flows and used to model DoD printing of viscoelastic inks [33]. The finite-element mesh is Lagrangian in nature; i.e., the nodes advect with the fluid flow.

To model the experiments it was assumed that the only body force acting on the fluid was gravity, and that there were no significant temperature variations, so that the fluid density and viscosity were constant. A cylindrical coordinate system $\{r,\theta,z\}$ was used to describe the jet, with the origin taken as the center of the nozzle outlet, and axisymmetry was assumed, i.e., independence of θ. The governing equations are the Navier-Stokes equations:

$$\rho\frac{\mathrm{D}\mathbf{u}}{\mathrm{D}t} = -\nabla p + \eta\nabla^2\mathbf{u} + \rho g\hat{\mathbf{z}}, \qquad \nabla\cdot\mathbf{u} = 0,$$

where ρ is the fluid density, t is time, $\mathbf{u}$ is the fluid velocity, p is the fluid pressure, and g is the acceleration due to gravity. Here $\mathrm{D}\mathbf{u}/\mathrm{D}t$ is the Lagrangian derivative, defined as $\mathrm{D}\mathbf{u}/\mathrm{D}t = \partial\mathbf{u}/\partial t + (\mathbf{u}\cdot\nabla)\mathbf{u}$. We scale lengths by the nozzle outlet radius $d/2$, velocities by the approximate drop speed upon reaching a steady near-spherical shape v, times by $d/2v$, and pressures and stresses by ρv^2. These scalings yield the dimensionless governing equations

$$\frac{\mathrm{D}\mathbf{u}}{\mathrm{D}t} = -\nabla p + \frac{1}{\mathrm{Re}}\nabla^2\mathbf{u} + \frac{1}{\mathrm{Fr}^2}\hat{\mathbf{z}}, \qquad \nabla\cdot\mathbf{u} = 0,$$

where t, $\mathbf{u}$, and p are now the dimensionless time, velocity, and pressure, respectively, Re is the Reynolds number as defined earlier in Sec. II B, and Fr is the Froude number, given by $\mathrm{Fr} = \sqrt{2v^2/gd}$. The value of the $1/\mathrm{Fr}^2$ factor is 0.022 for the experimental parameters. The boundary conditions are given in Sec. III B.

Drag due to air resistance was neglected in the simulations—using established empirical formulas [34], the deceleration due to air resistance was estimated to be less than 0.2 m s^{-2} for the drop sizes and speeds considered. Fitting quadratic curves through the experimental data obtained by high-speed imaging (droplet tip position versus time, considering only times by which the droplet had attained a near-spherical shape) yielded a free-fall acceleration of approximately 9.7 m s^{-2}, in agreement with the above estimate.

The velocity and pressure fields were discretized over a mesh of irregular triangular $P_1 - P_1$ Galerkin elements; they were assigned values at each mesh node, and their values elsewhere were determined through linear interpolation.

An artificial stabilization was employed in order to prevent spurious numerical pressure oscillations: the value of the stabilization parameter was optimized with respect to the spectral properties of the discrete coefficient matrix [32]. A theta scheme was used for the discrete time stepping, and the resulting difference equations were linearized via Picard iteration. Within each iteration, the linear system was solved numerically by the minimal residual (MINRES) method [35]. The size of the time step δt was adaptively restricted by a CFL condition of the form $U\delta t < \delta x$, where U is a typical flow velocity and δx is a typical element size. The position of each mesh node (except those on the printhead inlet boundary) was updated after each time step using the converged velocity solution for that node. The nodes on the printhead inlet present a special case: Their positions were held constant in order to preserve the printhead shape and the applicability of the velocity pulse boundary condition (see Sec. III B).

To maintain element shape quality throughout the simulations, local mesh reconnections were made between time steps in regions where significant element distortion had occurred. The criteria for reconnection were based on the attainment of the Delaunay triangulation, which is optimal in two dimensions for a given set of node positions and can be efficiently obtained from any initial triangulation [36]. The local mesh resolution was also maintained by the addition of new nodes in depleted regions, and the removal of nodes in congested regions.

Both computationally and theoretically, the study of the breakup of fluids is highly challenging. As breakup is approached, the thickness of the filament diminishes, and the fluid in the pinch-off region is driven by increasingly strong forces due to surface tension [8]. As the velocity goes to infinity due to the tension on the surface, a singularity of the equations of motion develops. In the final stages of capillary breakup every viscous fluid asymptotically approaches a universal thinning law proportional to the time remaining until breakup [37], independently of the particular conditions of the global flow. This has been experimentally observed for several fluids where the breakup is similar in the pinch-off region regardless of the initial conditions [8].

In this work, in order to simulate the capillary breakup of the fluid thread connecting the main droplet to the printhead, the fluid domain was subdivided when the thread radius fell below a certain threshold (here taken as $< 1\%$ of the nozzle outlet radius). No method of coalescence was implemented in the simulations. The choice of a finite threshold means that the final pinch-off dynamics of the jet are not fully represented in the simulations. To assess the importance of this, we show in Fig. 6 the minimum jet radius (at the neck) plotted against the time remaining before breakup Δt, with no threshold imposed. In addition to the case relevant to the experiments in this work (Oh $= 0.36$) a second, less viscous case (Oh $= 0.01$) is also shown. The value of the breakup time in each case was extrapolated from a linear fit to the final half decade of data points. For the Oh $= 0.36$ case, the neck radius was found to be linearly dependent on Δt as breakup is approached. The straight line fit (dashed in Fig. 6) has equation $0.03057\sigma\,\Delta t/\eta$, which is in agreement with the asymptotic Navier-Stokes pinch-off solution first obtained by Eggers [37]. For the Oh $= 0.01$ simulation, the neck radius

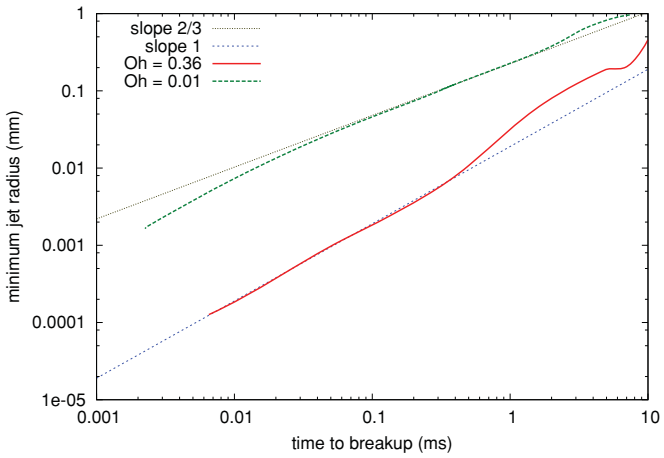

FIG. 6. (Color online) The variation of the minimum jet radius with the time until breakup, as a log-log plot. Simulation results are plotted for two Ohnesorge numbers of 0.36 (corresponding to the fluid used in the experiments) and 0.01, a far less viscous fluid. For the former a linear dependence was found as breakup was approached, whereas for the latter a 2/3 power law is followed transiently before deviation close to breakup. The breakup time for each case was extrapolated via linear fits to approximately the last half decade of data points.

follows a power law proportional to roughly $\Delta t^{2/3}$ for about two decades, before deviating toward a slower rate of thinning. The 2/3 power is consistent with the inviscid pinch-off solution described in Ref. [38]. In this simulation (unlike the previous one), the breakup time occurs while the driving velocity pulse is still in progress, and consequently there is non-negligible motion of the meniscus around the breakup region during the period prior to breakup. Thus it should be noted that this Oh $= 0.01$ case is not precisely equivalent to that of a free jet undergoing capillary breakup. Theoretically a free jet with low Ohnesorge number would follow the 2/3 inviscid law initially, before a transition toward the Navier-Stokes linear pinch-off law, which is followed until the continuum limit is reached (see Ref. [39] for a detailed review). In practice, small perturbations would cause secondary capillary instabilities to develop along the thinning filament and enhance breakup.

With regard to the present study, these detailed pinch-off dynamics are not of great consequence other than to verify that the numerical method is capable of reproducing capillary thinning on a finer scale, and to establish a suitable value for the cutoff threshold. When a finite threshold is imposed, it is important to choose its value appropriately to ensure that the thinning dynamics have been captured to a sufficient extent. In particular, the threshold should be reached only after the thinning has proceeded into the Navier-Stokes inertial-viscous pinch-off regime described previously. An early cutoff can result in a misrepresentation of the local jet shape in the pinch-off region, which could lead to a more global inaccuracy such as the erroneous formation of a satellite drop that would not have formed in the true flow (or vice versa). Imposing a threshold of 1% causes the breakup to be detected about half a millisecond before it would naturally occur (based on Fig. 6). This early breaking does not affect the position of the front end of the jet (i.e., the leading droplet), which is of primary

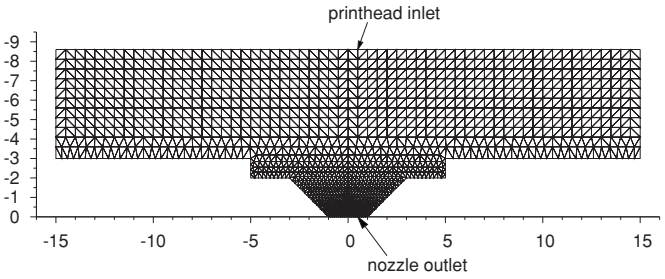

FIG. 7. The initial grid used in the simulations. Axisymmetry was assumed, so that only half of the displayed domain was simulated. The unit of length was 1 mm.

interest in this work, but rather only the precise length of the tail immediately after breakup.

B. Boundary conditions

The shape of the printhead used in the simulations was chosen to replicate the dimensions of the experimental conical nozzle, while simplifying the interior of the printhead behind the nozzle. The initial finite-element grid is shown in Fig. 7. The top boundary of the grid is the printhead inlet, at which the time-dependent velocity boundary condition

$$\mathbf{u} = \alpha V_P(t)\hat{\mathbf{z}} \quad \text{at } z = -8.6, \tag{2}$$

was imposed to represent the action of the piston motion in the experiments; here $V_P(t)$ is the velocity pulse function, and α is a scaling factor (see below). The bottom boundary of the grid is the nozzle outlet ($z = 0$). The initial shape of the fluid meniscus was flat (as in the experiments). The remaining boundaries of the grid ($-8.6 < z < 0$) are the rigid interior walls of the printhead and nozzle, at which boundary conditions of no slip were imposed ($\mathbf{u} = \mathbf{0}$). Axisymmetry about the z axis (the jet axis) was assumed throughout; the boundary conditions $\mathbf{u} \cdot \hat{\mathbf{r}} = 0$ and $\hat{\mathbf{r}} \cdot \boldsymbol{\tau} \cdot \hat{\mathbf{z}} = 0$ were applied at the jet axis $r = 0$, where $\boldsymbol{\tau}$ is the stress tensor. However, in the figures presented in Sec. IV we show reflected snapshots of the simulated domain for clarity in comparison with experimental photographs.

The boundary conditions at the free surface are those of zero shear stress and the interfacial pressure discontinuity due to the surface curvature

$$\hat{\mathbf{n}} \cdot \boldsymbol{\tau} \cdot \hat{\mathbf{t}} = 0 \text{ and } [\boldsymbol{\tau} \cdot \hat{\mathbf{n}}]_{\text{air}}^{\text{jet}} = -\frac{1}{\text{We}}\left(\frac{1}{R_1} + \frac{1}{R_2}\right)\hat{\mathbf{n}},$$

where $\hat{\mathbf{n}}$ is the unit vector normal to the free surface (directed outward from the jet), $\hat{\mathbf{t}}$ is the unit tangent vector to the free surface in the rz plane, We is the Weber number defined earlier in Sec. II C, and R_1 and R_2 are the principal radii of curvature[1] of the interface. It was assumed that the external air pressure was a negligible constant. The location of the interface in the rz plane (initially at the flat meniscus at $z = 0$) was determined implicitly via a kinematic condition: If the interface is represented as a parametric curve $\mathbf{x}(s,t)$, where s is some parameter, then its evolution is computed as $\partial\mathbf{x}/\partial t = \mathbf{u}$. In the simulations this was realized automatically, since the mesh was Lagrangian and the mesh nodes (including those on the interface) are advected with the local fluid velocity. The contact line between the interface and the interior walls of the nozzle was held pinned at the edge of the nozzle outlet. The fluid within the printhead was assumed to be initially at rest ($\mathbf{u} = \mathbf{0}$).

[1]The convention used here is that a radius of curvature is positive if its corresponding center of curvature lies on the jet side of the interface.

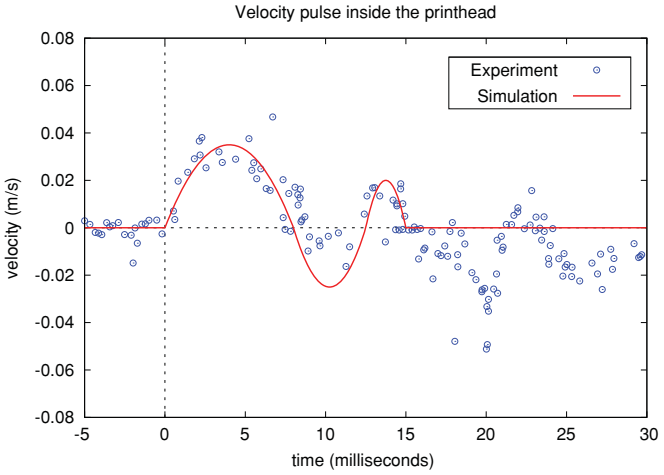

FIG. 8. (Color online) The vertical velocity pulse waveform $V_P(t)$ applied at the printhead inlet in the simulations (solid line), obtained by fitting a piecewise parabolic "push-pull-push" curve through the accumulated LDA data (circles).

In order to generate droplets in the simulations, a time-dependent vertical velocity pulse was prescribed uniformly at the printhead inlet. While this was not expected to accurately model the experimental flow throughout the entire printhead, it was designed to produce sufficiently similar flow conditions in the vicinity of the nozzle cone to yield a good correspondence between simulated and experimental drop shapes and speeds. The waveform of the pulse [i.e. the function $V_P(t)$ in the inlet boundary condition (2)] was determined by fitting a simplified piecewise parabolic "push-pull-push" curve through the experimental velocity data obtained by LDA measurements (i.e., the accumulated data shown in Fig. 5), and then shifting in time to define the onset of the first "push" as zero on the time axis. The shifted curve is shown in Fig. 8 together with the shifted LDA data. Note that in our coordinate system the positive direction is downward. After the end of the second "push" (at approximately 15 ms), the pulse was switched off and $V_P(t)$ was zero for the remainder of the simulation. Some trial cases were conducted with an additional "pull" phase in the pulse, but these did not show significantly different drop speeds or shapes and only marginally enhanced the rate of thinning of the ligament connecting the main drop to the printhead.

Having defined the shape of the pulse waveform, its amplitude was scaled by an overall factor α [see Eq. (2)] in order to calibrate the simulation results with the experiments. This was necessary in order to permit the simplifications discussed above, regarding the printhead shape and the means of drop generation in the simulations. The calibration was based on the position of the droplet tip upon detachment

from the printhead, and the approximate time at which that detachment occurred. Typical values for α were in the range 8%–9%.

IV. RESULTS

A graph of the droplet tip position versus time, measured vertically downward from the nozzle outlet, is shown in Fig. 9. Values are plotted for each time step in the simulation; the size of the time step was below 10 μs on average. The scale factor in the velocity pulse waveform was 8.4% for this simulation. The experimental data shown in Fig. 9 consist of measurements obtained through digital analysis of the single-flash photographs, using the method described in Ref. [4]. The photographs, each of which shows a separate droplet, were taken at successively later times after actuation, with an increment of 3 ms. Each individual photograph had an associated timing error of up to 2 ms, though this tolerance is likely to be a severe overestimate at early times.

Figure 9 shows good agreement between the simulation and the experiment at early and intermediate times. The droplet detached from the printhead at 19.0 ms in the simulation, and at approximately 20 ms in the experiment, comfortably within the interval of best agreement. At later times the two datasets begin to deviate; the onset of the deviation occurs at roughly the same time (approx. 33 ms) at which the tail of the droplet was fully absorbed by the main bulk. Around this time, the gradient of the tip position curve is enhanced slightly by the extra momentum received from the retraction of the tail. Subsequently, the results describe the free fall of a near-spherical drop subject to gravity and air resistance. The neglect of the latter in the simulation does not fully account for the apparent difference in acceleration during free fall. Indeed, fitting a quadratic through the last few experimental data points (ignoring error bars) gave an acceleration estimate of approximately 8 m s^{-2}, significantly lower than gravity minus the upper bound for air resistance (see Sec. III A). This suggests that the actual sizes of the timing errors may have been

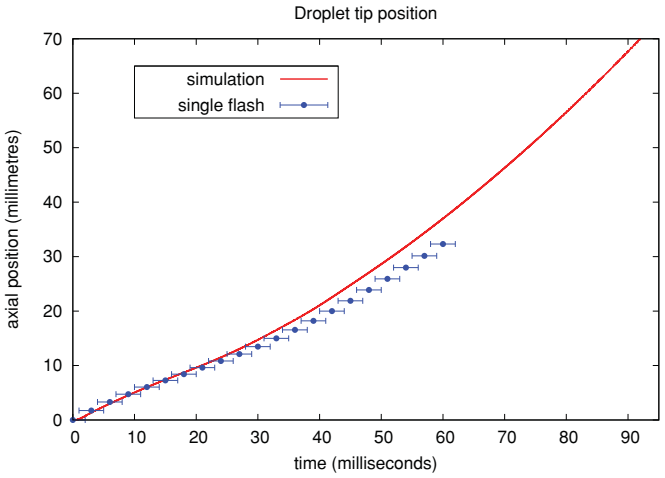

FIG. 9. (Color online) The droplet tip position, measured axially from the nozzle outlet, plotted vs. time. The simulation is compared with measurements taken from the single-flash photographs. Error-bars of ±2 ms in the latter are associated with potential inaccuracies in the flash timing.

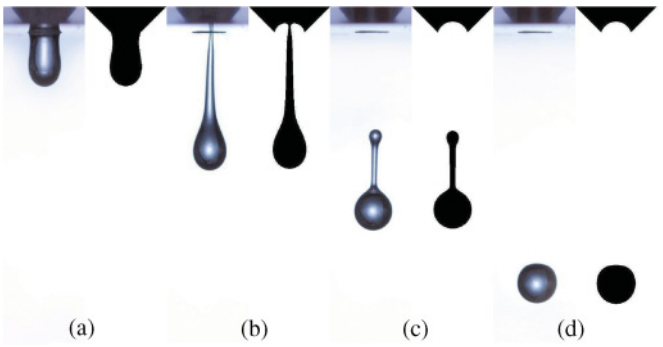

FIG. 10. (Color online) Single flash images from the experiments (as in Fig. 3) shown alongside their nearest matching simulation plots. The flash images were taken at approximate times of (a) 6 ms, (b) 18 ms, (c) 27 ms, and (d) 36 ms, with associated potential timing errors of ±2 ms. The simulation plots correspond to times of (a) 6.75 ms, (b) 17.75 ms, (c) 25.75 ms, and (d) 34.0 ms.

substantially larger at late times than at early times (though still within the given error bars). This issue was a principal motive for the use of the high-speed camera as a secondary visualization system.

A comparison of the droplet shapes is shown in Fig. 10. In each pair of images (a)–(d), the single-flash photograph is on the left and the simulation plot is on the right (the photographs are cropped versions of those shown earlier in Fig. 3). There is a close correspondence between the drop shapes computed in the simulation and those observed in the experiment. The apparent difference between the nozzle cone angles in adjacent images is due to refraction in the perspex. The pairing of images was done as follows: For each photograph, the corresponding simulation plot was chosen to be the one with the most similar droplet shape, considering only times within the error bars of the experimental flash timing. The simulation was set to output plots of the droplet shape at intervals of 0.25 ms. The greatest difference between the times of the paired images occurs for pair (d), which may be interpreted as a further indication that the flash timing errors were larger at later times, as mentioned above.

The four pairs of images (a)–(d) illustrate key stages in the evolution of the drop shape. Image pair (a) shows the initial protrusion of ink ejected from the nozzle during the first "push" phase in the driving pulse. The subsequent "pull" phase formed a drawn out filament behind the rounded main drop, as seen in (b). The filament underwent capillary thinning, the rate of which was influenced only slightly by further oscillations in the pulse, and broke at a point within the printhead. The tail end of the detached filament then recoiled and became rounded under surface tension, as shown in (c); the recoil gave the tail bead a faster downward speed than the main drop, resulting in the shortening of the connecting ligament. There was then competition between the capillary thinning of the ligament and the shortening as the tail bead approached the main drop. In this case the time for full retraction of the tail was shorter than the time for breakup of the ligament, and consequently a single drop was formed (d). The surface of this drop exhibited small decaying oscillations in the immediate aftermath of the absorption of the tail, before settling toward a

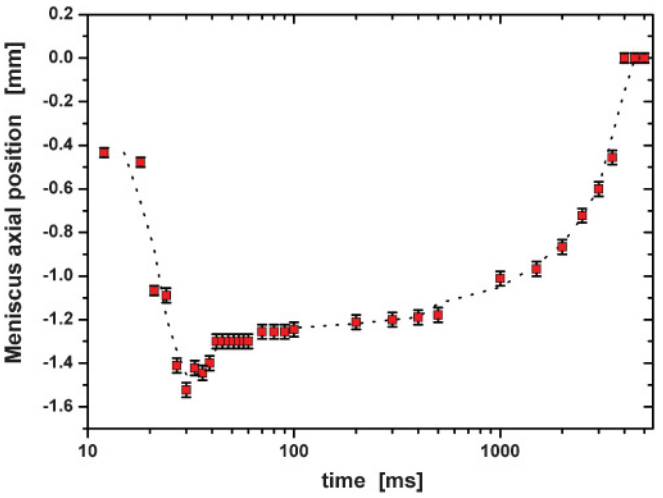

FIG. 11. (Color online) The vertical position of the center of the meniscus within the printhead. The droplet detached from the printhead at approximately 20 ms.

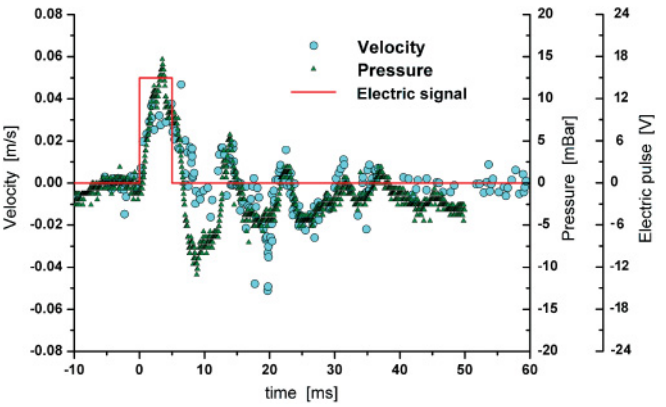

FIG. 12. (Color online) The pressure and velocity response inside the printhead. The electric signal sent to the actuator is shown in a solid line.

steady near-spherical shape (only differing from a true sphere due to air resistance).

A very slight asymmetry is visible in photographs (b) and (c) due to "tail hooking"—the meeting point of the tail filament and the meniscus in the nozzle was not precisely on the axis, causing minor deviation of the tail upon detachment. It has been suggested that this asymmetric breakup is likely to exist in setups where a single electric pulse is used as a driving waveform for DoD systems [12]. An important point to observe is that although the large-scale system used in this work does not use a piezoelectric driver, and the pressure or velocity waveforms do not consist of single pulses; the driving waveform is a single pulse. As a result, this asymmetric breakup is consistent with previous observations [12].

As mentioned earlier, the position of the meniscus within the nozzle was discernible in the single-flash photographs from 12 ms onward (see Fig. 3) and was measured directly from those photographs. A graph of these measurements is shown in Fig. 11. The time axis is on a logarithmic scale; the timescale of the driving pulse (and hence the droplet generation) is contained within the first decade. The droplet detached from the meniscus at 20 ms, and by around 40–50 ms the oscillations in the driving pulse had died down, resulting in a steady meniscus position thereafter. Subsequently, to prepare the experimental apparatus for the next actuation, the meniscus was gradually reset to its initial position (flat across the nozzle plane), as can be seen in the later two decades of the graph. A time of around 5 s was required for this reset.

No comparison was made between the experimental results of Fig. 11 and the meniscus position in the simulation. A quantitative comparison would have required the incorporation of further details of the printhead apparatus (beyond those described in Sec. III B) in order to model the resetting of the meniscus to the nozzle plane. It would also have been necessary to append further oscillatory phases to the driving velocity pulse, resulting in a more complex waveform than the simplified version shown in Fig. 8.

The fluid pressure within the printhead was recorded by the pressure transducer, and the measurements are shown in Fig. 12 together with the velocity data (acquired by LDA) and the electric signal sent to the loudspeaker. The further oscillations after the initial pulse are clearly visible in the pressure waveform, approximately in phase with the velocity. As these oscillations decayed, the pressure settled toward a steady value lower than the initial pressure prior to actuation, the difference being due to the loss of the ejected ink and the withdrawn meniscus. The pressure was then gradually raised back to its initial value by the movement of the meniscus, in order to restore the initial conditions of the experiment (as discussed above).

To avoid the timing errors inherent in the single-flash photography method, continuous high-speed imaging was also used to provide an alternative method of visualization. In a separate series of experiments, the drop generation apparatus was therefore used in a slightly modified configuration, and the following results therefore represent a separate case, slightly different from the case presented above. The droplet generator was dismantled for cleaning and then reassembled prior to this second series of experiments. Therefore the precise position of some of its components and their wettability may have been slightly altered. Although the fluid and nozzle properties and the electric and pressure waveforms remained unchanged, the jetting behavior was slightly modified as the creation of a satellite droplet was observed.

The improved timing accuracy afforded by the high-speed camera allows better quantitative comparison between the experiment and simulation, as shown in the graph of the droplet tip position versus time in Fig. 13. The experimental data were obtained by direct measurement of the images; the resolution and contrast provided by this method of imaging were, however, insufficient to permit the same methods of digital analysis as those applied to the single-flash photographs.

As in the comparison with the single-flash photographs, the tip position results in Fig. 13 agree best for early and intermediate times. The simulated droplet was slightly in front over the first 10 milliseconds, but after this the two droplets matched very closely up until detachment (at 18 ms) and beyond. This was expected of course, as the tip position upon detachment from the nozzle was one of the criteria used to calibrate the scale factor amplifying the driving pulse (see Sec. III B), which was 8.35% for this simulation. The results

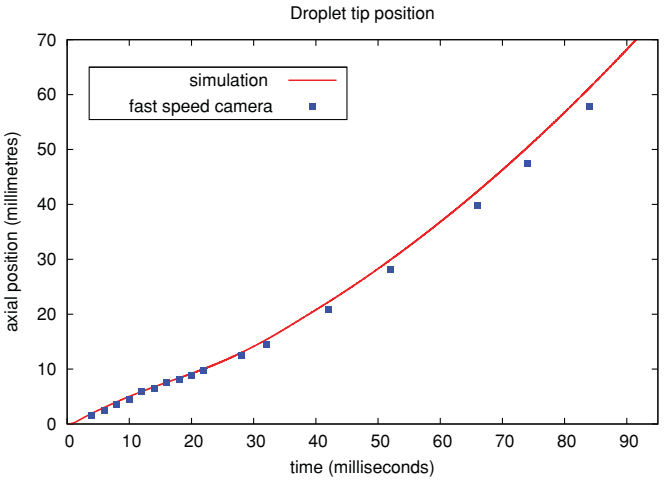

FIG. 13. (Color online) The droplet tip position, measured axially from the nozzle outlet, plotted vs. time. The simulation is compared with measurements taken from the high-speed camera images.

first start to diverge at about 30 ms, just after the tail of the simulated droplet had fully retracted into the main drop, increasing its momentum and causing it to move ahead of the experimental droplet. In this experiment the droplet tail did not fully retract; instead the tail bead broke away just before absorption could occur and was deflected sideways as a secondary "satellite" drop, as can be seen from the later two images in Fig. 14. Therefore the experimental drop did not acquire the full momentum of the tail and was consequently slower thereafter than the simulated drop. It is worth noting that an additional simulation in which the droplet tail bead was artificially removed at 28 ms resulted in significantly closer agreement with the experimental tip position measurements at later times, thereby resolving some of the discrepancy in Fig. 13.

High-speed images and simulation plots are juxtaposed at equal times in Fig. 14. It should be emphasized that, unlike the single-flash photographs, each of the high-speed images shows the same droplet. The droplet shape development shown in the first four image pairs (a)–(d) is qualitatively the same as that observed in the previous comparison with the single-flash photographs. The two images in each of the first four pairs agree closely, apart from the slightly slower tail-recoil upon detachment in the experiment, which caused the tail to shorten less rapidly than in the simulation. However, the last two image pairs (e) and (f) show clearly that in this experiment the tail bead did not merge with the main drop upon collision, instead continuing as a separate satellite drop. This behavior was observed repeatedly over many consecutive actuations. The lack of coalescence seems to have been caused primarily by the oblique nature of the collision, due to tail hooking (i.e., asymmetry upon detachment), rather than by any capillary breakup of the connecting ligament prior to the collision. Indeed, the droplet shapes in the high-speed images (b)–(d) are substantially less axisymmetric than those observed in the previous experiment via single-flash photography (see Fig. 10), whereas, at similar times, the ligament was relatively shorter compared with the previous case, allowing less time for pinch-off to occur. In simulations, satellite drops formed

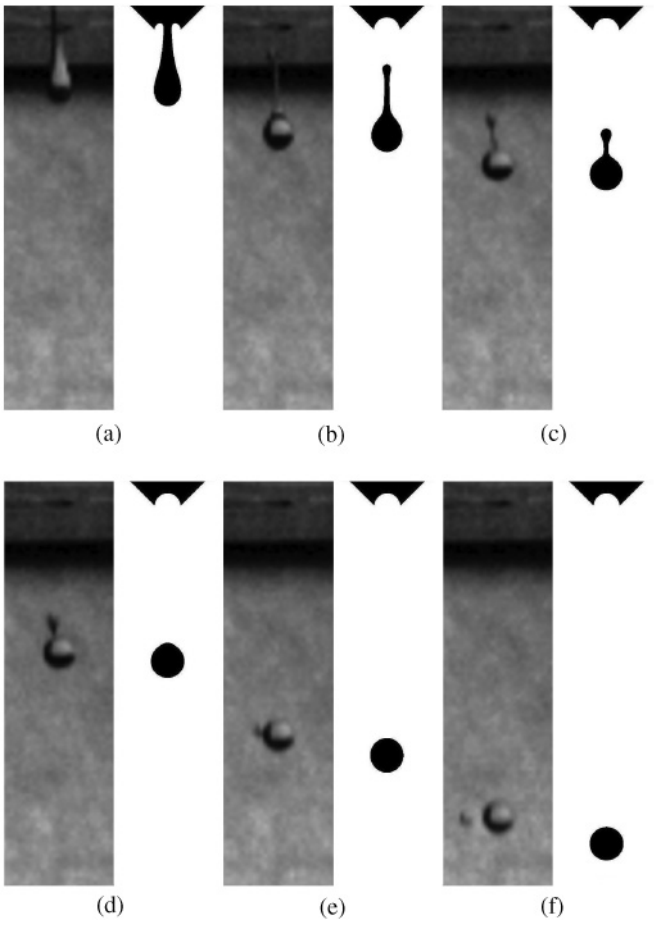

FIG. 14. High-speed images from the experiment shown alongside their corresponding simulation plots, at times of (a) 12 ms, (b) 22 ms, (c) 28 ms, (d) 30 ms, (e) 42 ms, and (f) 52 ms.

by ligament breakup were observed only when the scale factor α in the driving pulse amplitude was greater than 8.7%.

All experiments and simulations were performed with an Ohnesorge number lying in the region identified as critical by previous studies [16,24]. This critical region [Oh $\approx$ O(0.1)] governs the breakup of a free liquid ligament, which is in this case formed during the jetting process. Although the internal dynamics and the geometry of the filament of a jetted droplet are not exactly represented by the idealized models used for the derivation of the critical Ohnesorge number [16,24], the model stands for long filaments of high viscosity regardless of the initial internal motion [24]. As previously mentioned, two series of experiments and simulations were performed for this work. In the first series of experiments with conventional shadowgraphy the filament of the jetted droplet did not break up, and coalescence of the tail and the main drop was observed; this is shown in Fig. 15. In contrast, although performed under the same values of the Re, We, and Oh numbers, the experiments with high-speed imaging presented the breakup of the droplet filament into a satellite droplet. This suggests that our experiments were conducted in a borderline regime where the breakup is susceptible to slight fluid and flow changes. This was also observed in the simulations and is in agreement with previous results [10,16].

FIG. 15. (Color online) Shadowgraph images showing filament evolution; frames are separated by 3 ms, starting at 21 ms after actuation. The initial aspect ratio of the filament is $\gtrsim$15, and Oh = 0.36.

V. CONCLUSIONS

An experimental setup that is capable of producing millimeter-sized drops on demand, and that allows the direct measurement of both the velocity and the pressure inside this large-scale printhead, has been demonstrated and its results reported. A simple reconstruction process was applied to LDA-acquired velocity data in order to extract the velocity waveform within the printhead chamber that was induced by the action of a pressure pulse. The conditions required to produce droplets on demand—fluid properties, nozzle geometry, and the velocity waveform within the printhead—were directly measured in the experimental setup and then used as inputs to Lagrangian simulations. Two separate shadowgraph visualization systems were used for the comparison of experiments and simulations, and good agreement in the droplet shapes and positions was established, both qualitatively and quantitatively, thereby demonstrating the ability of the simulations to accurately replicate the creation and evolution of droplets of Newtonian liquids.

Potentially, this work establishes a method for the effects of the electrical drive signal on jet breakup to be studied in terms of fundamental properties of the flow within the printhead, such as the fluid velocity or the pressure wave. Future studies might aim to understand how more complex pressure waves, for example, with negative components, may change the breakup behavior by modifying the dynamics of the filament still connected to the fluid within the nozzle, as has been reported previously [11,17].

ACKNOWLEDGMENTS

This work was supported by EPSRC and the industrial partners in the "Next-Generation Inkjet Technology" project. The authors are grateful to M. R. Mackley for the loan of the LDA equipment. The authors also wish to thank the anonymous referees for their helpful comments.

[1] J. W. Strutt (Lord Rayleigh), *The Theory of Sound,* Vol. 2 (Macmillan and Co., London, 1894).
[2] F. Savart, Ann. Chim. **53**, 337 (1833).
[3] J. Eggers, in *Nonsmooth Mechanics and Analysis,* Vol. 12, edited by P. Alart, O. Maisonneuve, and R. T. Rockafellar (Springer, New York, 2006) p. 163.
[4] I. M. Hutchings, G. D. Martin, and S. D. Hoath, J. Imaging Sci. Technol. **51**, 438 (2007).
[5] H. Wijshoff, in *IS&T-NIP22: International Conference on Digital Printing Technologies* (Springfield VA, USA, 2006), p. 79.
[6] A. Asai, T. Hara, and I. Endo, Jpn. J. Appl. Phys. **26**, 1794 (1987).
[7] A. V. Bazilevskiy, J. D. Meyer, and A. N. Rozhkov, Fluid Dyn. **40**, 376 (2005).
[8] J. Eggers, Rev. Mod. Phys. **69**, 865 (1997).
[9] O. A. Basaran, Am. Inst. Chem. Eng. J. **48**, 1842 (2002).
[10] H. Dong, W. W. Carr, and J. F. Morris, Phys. Fluids **18**, 072102 (2006).
[11] Q. Xu and O. A. Basaran, Phys. Fluids **19**, 102111 (2007).
[12] A. U. Chen and A. Basaran, Phys. Fluids **14**, L1 (2002).
[13] C. D. Meinhart and H. Zhang, J. Microelectromech. Syst. **9**, 67 (2000).
[14] A. K. Sen and J. Darabi, J. Micromech. Microeng. **17**, 1420 (2007).
[15] A. S. Yang, C. H. Cheng, and C. T. Lin, J. Mech. Eng. Sci. **220**, 435 (2006).
[16] P. K. Notz and O. A. Basaran, J. Fluid Mech. **512**, 223 (2004).
[17] H. Dong, W. W. Carr, and J. F. Morris, Rev. Sci. Instrum. **77**, 085101 (2006).
[18] J. R. Castrejón-Pita, G. D. Martin, S. D. Hoath, and I. M. Hutchings, Rev. Sci. Instrum. **79**, 075108 (2008).
[19] Entran Sensors & Electronics, *EPX Pressure Sensors, Miniature Threaded Stainless Steel Diaphragm Specification Sheet* (Entran, Fairfield, NJ, 2008).
[20] H. J. Manning and R. A. Harvey, in *IS&T-NIP15: International Conference on Digital Printing Technologies* (Springfield VA, USA, 1999), p. 35.
[21] E. D. Wilkes, S. D. Phillips, and O. A. Basaran, Phys. Fluids **11**, 3577 (1999).
[22] R. L. Nasser, S. Chandra, and J. R. Andrews, Am. Inst. Chem. Eng. J. **54**, 3084 (2008).
[23] A. U. Chen, P. K. Notz, and A. O. Basaran, Phys. Rev. Lett. **88**, 174501 (2002).
[24] R. M. S. M. Schulkes, J. Fluid Mech. **309**, 277 (1996).
[25] J. Q. Feng, J. Imaging Sci. Technol. **46**, 398 (2002).
[26] D. González-Mendizabal, C. Olivera-Fuentes, and J. M. Guzmán, Chem. Eng. Comm. **56**, 117 (1987).
[27] T. Battal, C. D. Bain, M. Weiss, and R. C. Darton, J. Colloid Interface Sci. **263**, 250 (2003).
[28] R. J. Adrian, *Laser Velocimetry in Fluid Mechanics Measurements* (Hemisphere Publishing, New York, 1983).
[29] L. E. Drain, *The Laser Doppler Technique* (Wiley, Chichester, UK, 1986), p. 182.

[30] J. R. Castrejón-Pita, A. A. Castrejón-Pita, G. Huelsz, and R. Tovar, Phys. Rev. E **73**, 036601 (2006).
[31] Dantec, Product Information P1270003 (Dantec, Tonsbakken, Denmark, 2003).
[32] O. G. Harlen, J. M. Rallison, and P. Szabó, J. Non-Newtonian Fluid Mech. **60**, 81 (1995).
[33] N. F. Morrison and O. G. Harlen, Rheo. Acta **49**, 619 (2010).
[34] K. V. Beard and H. R. Pruppacher, J. Atmos. Sci. **26**, 1066 (1969).
[35] C. Paige and M. Saunders, SIAM J. Numer. Anal. **12**, 617 (1975).
[36] H. Edelsbrunner, Acta Numerica **9**, 133 (2000).
[37] J. Eggers, Phys. Rev. Lett. **71**, 3458 (1993).
[38] R. F. Day, E. J. Hinch, and J. R. Lister, Phys. Rev. Lett. **80**, 704 (1998).
[39] J. Eggers and E. Villermaux, Rep. Prog. Phys. **71**, 036601 (2008).